

# Flexoelectric Polarization Enhancement in Paraelectric BaHfO<sub>3</sub> via Strain Gradient Engineering

*Timo Piecuch<sup>1,2</sup>, Jeffrey A. Brock<sup>1,3</sup>, Xiaochun Huang<sup>1,2</sup>, Arnold M. Müller<sup>4</sup>, Christof Vockenhuber<sup>4</sup>, Christof W. Schneider<sup>1</sup>, Thomas Lippert<sup>1,2</sup>, Nick A. Shepelin<sup>1\*</sup>*

<sup>1</sup>Center for Neutron and Muon Sciences, Paul Scherrer Institute, 5232 Villigen PSI, Switzerland

<sup>2</sup>Laboratory of Inorganic Chemistry, Department of Chemistry and Applied Biosciences, ETH Zürich, 8093 Zurich, Switzerland

<sup>3</sup>Laboratory for Mesoscopic Systems, Department of Materials, ETH Zürich, 8093 Zurich, Switzerland

<sup>4</sup>Laboratory of Ion Beam Physics, ETH Zürich, 8093, Zürich, Switzerland

**Keywords:** BaHfO<sub>3</sub>, paraelectric, dielectric, strain gradient, flexoelectricity, thin film, perovskite oxide

## Abstract

Flexoelectricity - polarization induced by strain gradients - offers a route to polar functionality in centrosymmetric dielectrics, where traditional piezoelectric effects are absent. This study investigates the flexoelectric effect in epitaxial BaHfO<sub>3</sub> (BHO) thin films, a centrosymmetric and paraelectric perovskite. While a large lattice mismatch induces defect-driven relaxation, a coherently grown BHO film undergoes elastic relaxation, forming intrinsic strain gradients exceeding  $10^6 \text{ m}^{-1}$ . A 29-fold enhancement in spontaneous polarization is observed at an electric field of  $4 \text{ MV cm}^{-1}$  for BHO exhibiting a strain gradient compared to relaxed BHO. This enhancement is attributed to flexoelectric coupling, which is isolated from ferroelectric and piezoelectric contributions due to the centrosymmetric nature and the absence of phase transitions in BHO. The findings establish a clear link between engineered strain gradients and enhanced polarizability in oxide thin films, offering a benchmark system for deconvoluting the flexoelectric effect from other polar effects. These results provide a basis for exploiting flexoelectricity in dielectric devices and advance the fundamental understanding of strain-coupled phenomena in functional oxides.

## Introduction

Strain gradients play a fundamental role in determining the structural distortions that give rise to polar order, particularly at the nanoscale. In crystalline solids, strain gradients describe spatially inhomogeneous variations in strain, which can significantly influence physical properties such as polarization, defect dynamics, and phase stability.<sup>[1-4]</sup> Understanding and controlling these gradients is crucial for designing next-generation functional materials with tailored polar responses.<sup>[5,6]</sup>

In epitaxial thin films, the misfit strain is primarily governed by the lattice mismatch between the film and its underlying substrate or buffer layer, given by  $\epsilon=(a_f-a_s)/a_s$ , where  $a_f$  and  $a_s$  correspond to the in-plane lattice parameters of the film and the substrate, respectively.<sup>[7,8]</sup> In oxides, a lattice misfit strain above 1-2% typically leads to strain relaxation at the interface via the formation of structural defects (e.g., point defects and threading dislocations), driving the material toward its bulk lattice parameter (**Figure 1(a)**). Conversely, when the misfit strain is sufficiently small and the growth parameters are sufficiently optimized, the film remains coherently strained to the underlying lattice of the substrate. A coherent growth results in a gradual relaxation throughout the structure (**Figure 1(b)**), governed by the mechanical properties of the film. This strain evolution can introduce substantial strain gradients across the film thickness.<sup>[9-11]</sup>

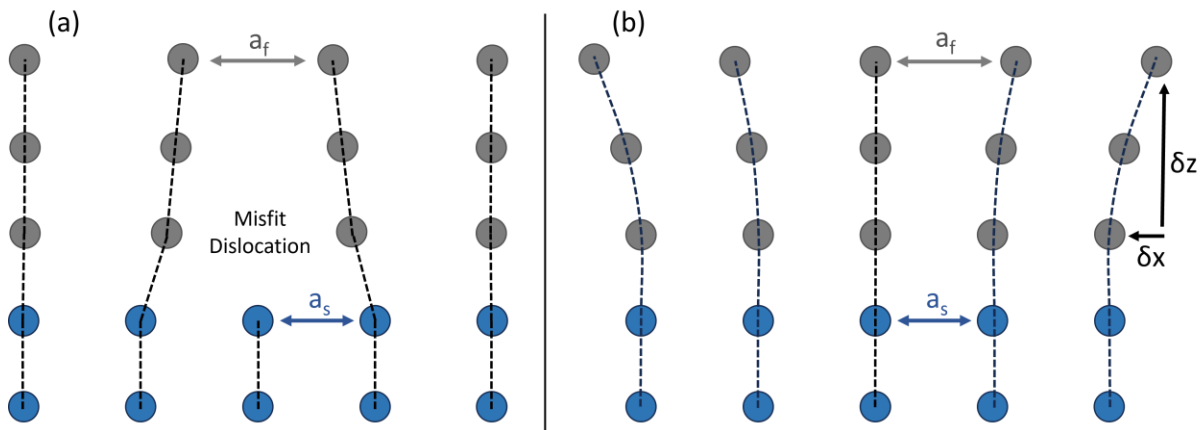


**Figure 1.** Schematic of a film (grey) grown on a substrate or buffer layer (blue), with lattice constants  $a_f$  and  $a_s$  respectively. In case of a large lattice mismatch (a), relaxation is mediated by the formation of misfit dislocations, while in the epitaxial case (b), strain relaxation occurs via a continuous strain gradient.

One of the most intriguing consequences of strain gradients in dielectric materials is the flexoelectric effect, a phenomenon in which a strain gradient induces electric polarization manifesting as bound surface charge.<sup>[1-4]</sup> Unlike piezoelectricity, which occurs only in non-centrosymmetric space groups and is an intrinsic property based on the chemical composition, flexoelectricity is an extrinsic effect that can be present in all compositions of dielectric materials, including centrosymmetric materials.<sup>[12-15]</sup> This makes it particularly attractive for applications requiring polarization in systems where conventional ferroelectric or piezoelectric materials are unsuitable due to chemical restrictions or structural incompatibilities. The flexoelectric effect holds potential for novel energy harvesting devices, tunable capacitors, and electromechanical sensors. Nevertheless, despite its fundamental importance, flexoelectricity has been largely overlooked due to its typically small magnitude in bulk materials.<sup>[1,5,6]</sup>

The flexoelectric coefficient is proportional to the strain gradient. Therefore, the potential of flexoelectricity is enhanced in epitaxial thin films, since elastic strain relaxation results in much larger strain gradients ( $10^6 \text{ m}^{-1}$  in this work) compared to relaxation over bulk scale (up to  $10^{-1} \text{ m}^{-1}$  in  $\text{SrTiO}_3$  (STO) single crystals).<sup>[1,16,17]</sup> An additional advantage of thin films is the precise control of the initial strain state, which is determined by the lattice mismatch between the film and the substrate.<sup>[7,8]</sup> The unique mechanical properties of perovskite oxides enable tunable strain gradients through elastic relaxation mechanisms. The ability to engineer and manipulate these strain fields in thin films opens new avenues for tuning material functionalities, particularly in electromechanical and dielectric applications.<sup>[18,19]</sup> For instance, research on tensile-strained  $\text{HoMnO}_3$  films has revealed strain gradients several orders of magnitude larger than those in bulk oxides, leading to significant flexoelectric responses.<sup>[20,21]</sup>

$\text{BaHfO}_3$  (BHO) emerges as an ideal model system for studying flexoelectricity in epitaxial oxide thin films due to its unique combination of properties. As a centrosymmetric perovskite crystallizing in the cubic  $Pm-3m$  space group, BHO eliminates the interference of linear and nonlinear dielectric effects, allowing for a clear distinction of flexoelectric contributions. The paraelectric nature of this material, with no known phase transitions, ensures stability across a broad range of temperatures, strain states and electric fields.<sup>[22]</sup> Additionally, the atomic planes in BHO (i.e.,  $\text{Ba}^{2+}\text{O}^{2-}$  and  $\text{Hf}^{4+}\text{O}_2^{2-}$ ) exhibit balanced charge distributions, eliminating polarization arising from charged plane contributions.<sup>[23]</sup> The material also exhibits a high dielectric constant, which enhances its potential for dielectric applications.<sup>[24]</sup> These properties, along with a pronounced mechanical stability, make it well-suited for integration into advanced electronic devices.<sup>[22,25]</sup>

To achieve a gradual strain relaxation throughout the film, the BHO films have been grown on STO (001) substrates buffered with epitaxially-grown LBSO that acted as the bottom electrode and set the interfacial strain to -1.2%. Symmetric capacitor structures have been prepared for electrical measurements. These results are compared to a BHO capacitor grown on a conductive  $\text{SrRuO}_3$  (SRO) buffer layer, corresponding to an interfacial lattice mismatch of -6.1%, which results in a misfit dislocation-driven relaxation at the SRO/BHO interface to release the strain. The strain states and strain gradients have been measured by high-resolution X-ray diffraction (HRXRD), and transmission electron microscopy (TEM) has been employed to locally verify the sharp interfaces with no signs of atomic diffusion between the layers. These analyses reveal pronounced strain gradients as the dominant relaxation mechanism in capacitors utilizing LBSO electrodes. To elucidate the polar behavior of both systems, temperature-dependent dielectric spectroscopy and polarization-electric field hysteresis measurements have been conducted. A striking 29-fold increase in spontaneous polarization was observed in comparison to capacitor structures exhibiting dislocation-mediated relaxation on an SRO bottom electrode, revealing the impact of strain gradient-driven flexoelectric effects.

This research provides a fundamental basis for achieving pronounced strain gradients along with significantly enhanced field-dependent polarization, in high-quality epitaxial BHO thin films. For the first time, such an investigation is conducted on a paraelectric, centrosymmetric material with no known phase transitions, offering a pathway to isolate and study pure flexoelectric effects without interference from ferroelectric or piezoelectric contributions.

## Results and Discussion

Symmetric capacitor structures were fabricated on STO substrates using two different bottom electrode materials. Each layer was grown *via* pulsed laser deposition (PLD), without breaking vacuum, under previously iteratively optimized conditions. As a reference, BHO was deposited on a conductive SRO buffer layer, corresponding to a large interfacial lattice mismatch of -6.1% (**Figure 2a**). In contrast, in the second configuration, BHO was epitaxially grown on LBSO, establishing an interfacial strain of -1.2% between the bottom electrode and the dielectric layer (**Figure 2b**). Reciprocal space mapping (RSM) analysis was conducted to elucidate the dominant strain relaxation mechanism in each structure, which formed the basis for the electrical characterization of the two systems.

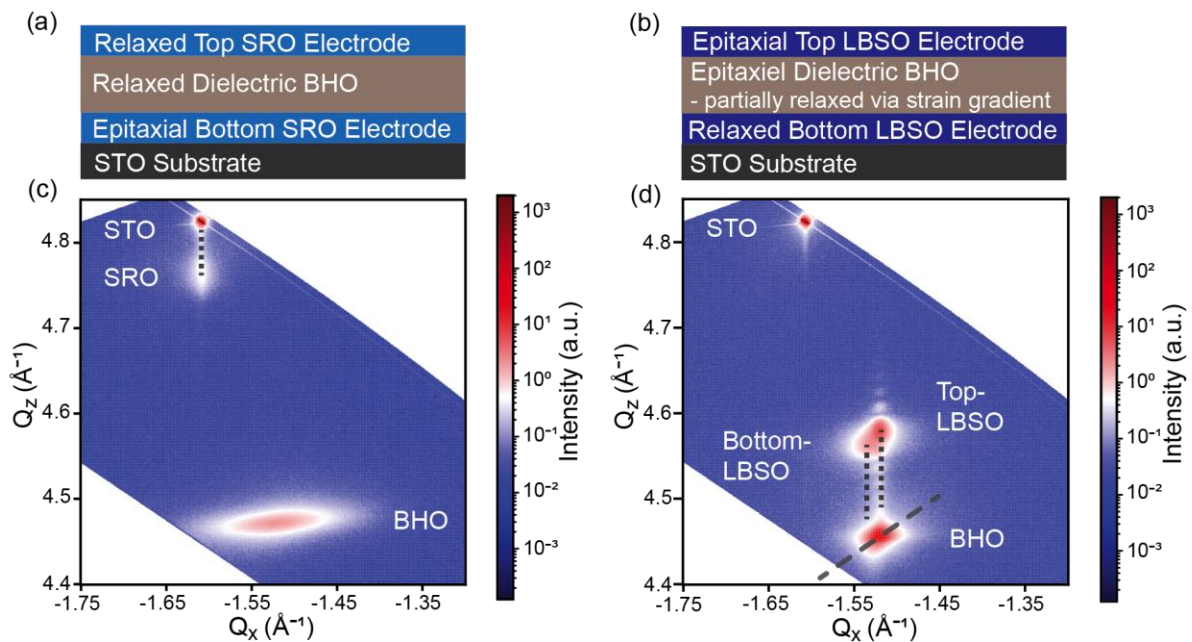


**Figure 2.** Schematic illustration of the (a) STO/SRO/BHO/SRO and (b) STO/LBSO/BHO/LBSO capacitor structure. The respective RSM's of the (-103) signal is shown in (c) and (d). The vertical dotted lines correspond to the in-plane lattice parameters for two adjacent strained layers, whereas the diagonal line in (d) corresponds to the theoretical relaxation line of BHO. Lattice parameter for top and bottom LBSO electrode layers are distinguishable due to a relaxation gradient in the BHO signal.

STO, BHO and LBSO have a cubic crystal structure, whereas SRO (orthorhombic) is treated as pseudocubic. Thus, the films were anticipated to grow with a cube-on-cube epitaxial relationship. The RSM measurements were performed for the asymmetric (-103) signal to achieve an improved signal-to-noise ratio, due to the low incidence angle of the X-ray beam. **Figure 2 (c)** displays the RSM along the asymmetric (-103) Bragg signal of the capacitor structure with an SRO bottom and top electrode. SRO strains in-plane to STO (exhibiting the same  $Q_x$  value), thus both peaks correspond to an in-plane lattice parameter of 3.91  $\text{\AA}$ . The SRO out-of-plane lattice parameter is 3.96  $\text{\AA}$ . The interposed BHO layer is fully relaxed according to the RSM and exhibits a lattice parameter of 4.15  $\text{\AA}$  in-plane and 4.22  $\text{\AA}$  out-of-plane. This position aligns with the fully relaxed

BHO structure grown directly on the STO substrate (**Figure S1**). The SRO top electrode is not visible in the RSM, indicating a reduced crystalline order due to growth on the fully relaxed BHO layer. These findings demonstrate that the dielectric BHO layer fully relaxes and does not accumulate residual strain when grown on SRO, due to the large lattice mismatch.

**Figure 2 (d)** shows the RSM of the capacitor structure with LBSO as both the bottom and top electrode. The fully relaxed bottom LBSO signal (in-plane 4.10 Å and out of plane 4.13 Å) is distinguishable from the top LBSO signal (in-plane 4.14 Å and out of plane 4.11 Å). The BHO layer strains to the bottom electrode and relaxes along the theoretical relaxation line (the dashed diagonal line overlaid on the BHO peak in **Figure 2 (d)**) based on the Poisson ratio of 0.25.<sup>[24]</sup> Such a relaxation profile corresponds to the elastic relaxation of the BHO.<sup>[26,27]</sup> The top LBSO electrode aligns with the partially relaxed BHO structure. The in-plane lattice parameter difference in the RSM between the bottom and top LBSO layers creates a 1% strain across the 100 nm BHO layer, corresponding to a strain gradient of approximately  $10^6 \text{ m}^{-1}$ .

The high epitaxial quality of BHO is further verified by an HRXRD  $2\theta$  line-scan and the corresponding rocking curve (**Figure S2**). Atomic force microscopy (AFM) and reflection high-energy electron diffraction (RHEED) measurements confirm the controlled layer-by-layer growth mode (**Figure S3**), showing an atomically-flat film surface characterized by vicinal terraces that correspond to one unit cell in step height and a streaky profile exhibiting intensity oscillations during growth, respectively.

TEM measurements were performed to verify the strain relaxation mechanisms inferred from the RSMs. **Figure 3 (a)** presents a low-resolution cross-sectional image of the two prepared capacitor structures. It should be noted that, for practical reasons, the second sample employs an LBSO top electrode instead of a symmetric SRO/BHO/SRO configuration; however, this modification does not affect the analysis or interpretation of the results. Elemental mapping confirms the uniform distribution of oxygen across both samples (**Figure 3 (b)**). Strontium (Sr) is primarily localized in the substrate and SRO electrode, but is also detected as a minor contaminant within the dielectric BHO and conductive LBSO layer (**Figure 3 (c)**). This contamination is likely attributed to impurities in the respective targets, particularly considering that the Sr signal of the LBSO buffer layer is weaker than that of the BHO, thus interdiffusion of Sr from the substrate is not likely to occur. Distinct elemental signatures enable the clear identification of the layers: LBSO is characterized by the presence of tin (Sn) (**Figure 3 (d)**), BHO by hafnium (Hf) (**Figure 3 (e)**), and SRO by ruthenium (Ru) (**Figure 3 (f)**). A high-resolution TEM (**Figure 3 (g)**) reveals that the BHO layer exhibits coherent epitaxial strain when grown on LBSO. In contrast, at the interface with the bottom SRO, numerous defects are observed in the interface-near region of the BHO, indicating that strain relaxation primarily occurs through the formation of misfit dislocations. These findings are consistent with the strain behavior deduced from the RSM analysis.

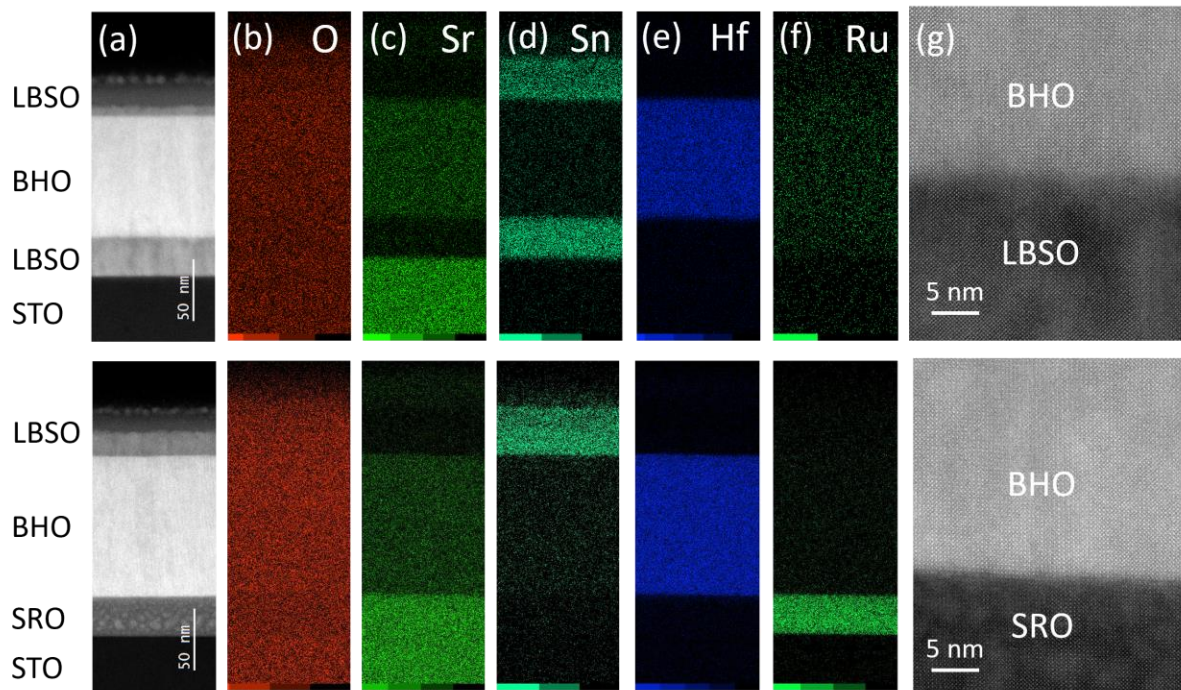


**Figure 3.** Cross-sectional TEM analysis of the capacitor structures: **(top)** STO/SRO/BHO/LBSO and **(bottom)** STO/LBSO/BHO/LBSO. **(a)** Low-resolution TEM overview image of both structures. **(b–f)** Elemental mapping of **(b)** O, **(c)** Sr, **(d)** Sn, **(e)** Hf, and **(f)** Ru, enabling identification of the individual layers. **(g)** High-resolution TEM image of the bottom-electrode/BHO interface.

To confirm the absence of phase transitions in BHO, the relative permittivity ( $\epsilon$ , **Figure 4 (a)**) and dielectric loss ( $\tan(\delta)$ , **Figure 4 (b)**) were measured as a function of both temperature and frequency for the STO/LBSO/BHO/LBSO capacitor structure, in which the BHO layer is coherently strained to the LBSO and partially relaxed via a strain gradient. At frequencies below  $2 \times 10^3$  Hz, increased noise levels are observed, as expected for low-frequency measurements.<sup>[28,29]</sup> Across the investigated temperature range from 50 K to 800 K, relative variations in the dielectric constant remain below 3.8%, and variations in dielectric loss remain below 3.0 %, indicating the absence of phase transitions in the BHO layer.

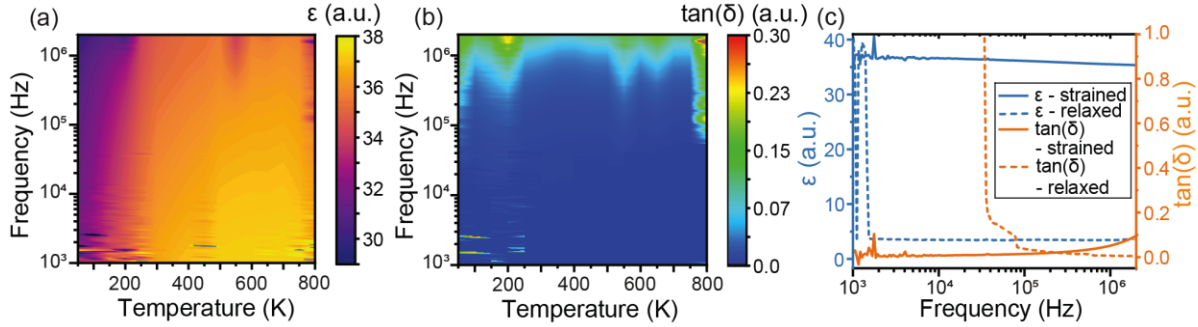


**Figure 4.** (a) Relative permittivity ( $\epsilon$ ) as a function of frequency and temperature. (b) Dielectric loss ( $\tan(\delta)$ ) as a function of frequency and Temperature. (c) Relative permittivity (blue) and dielectric loss (orange) at 450 K for the fully relaxed BHO structure grown on SRO (dashed line) and BHO strained to LBSO, partially relaxed via a strain gradient (solid line).

Furthermore, a direct comparison was performed at 450 K between the STO/LBSO/BHO/LBSO and STO/SRO/BHO/SRO capacitor structures (**Figure 4 (c)**). For the structure with BHO strained to LBSO, the relative permittivity remains stable across the entire measured frequency range, with only a slight increase in dielectric loss near  $10^6$  Hz. In contrast, the device incorporating a fully relaxed BHO layer grown on SRO exhibits significantly higher dielectric losses at low frequencies, which decrease as the frequency approaches  $10^6$  Hz. This behavior suggests the presence of additional defect-mediated conduction pathways in the relaxed BHO layer. Moreover, the relative permittivity of the relaxed structure is more than four times lower than that of the strained system for frequencies above  $2 \times 10^3$  Hz. These results indicate a substantial enhancement of the dielectric response in the strained BHO layer.

Notably, the dielectric constant of the fully relaxed system is more than four times lower than values reported in previous studies.<sup>[23,24]</sup> This deviation is attributed to an off-stoichiometry in the Ba:Hf ratio, with a deficiency for Ba corresponding to approximately 15%, as determined by Rutherford backscattering spectrometry (RBS) (**Figure S4**). Such A-site cation deficiencies have been widely associated with pronounced alterations in the dielectric response of thin-film perovskites. Furthermore, this stoichiometric imbalance may account for the observed deviation from ideal tetragonality in the relaxed BHO (**Figure 1 (c)**, **Figure S1**), which would otherwise be expected to equal one for a cubic perovskite material.<sup>[30-33]</sup>

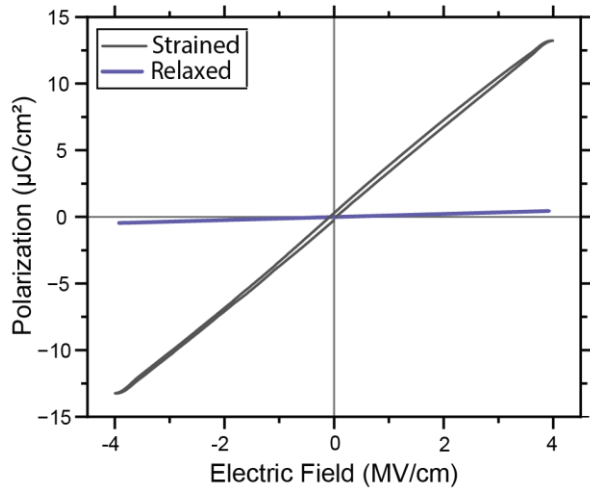


**Figure 5.** P-E hysteresis loop for the STO/SRO/BHO (fully relaxed)/SRO structure and the STO/LBSO/BHO/LBSO structure, with BHO strained to LBSO, partially relaxed via a strain gradient.

**Figure 5** presents the polarization-electric field (P-E) hysteresis loops for both capacitor structures. The STO/SRO/BHO/SRO device exhibits a maximum polarization of  $0.45 \mu\text{C cm}^{-2}$  at an applied field of  $4 \text{ MV cm}^{-1}$ , consistent with the expected linear dielectric behavior of a paraelectric material. In contrast, the STO/LBSO/BHO/LBSO structure, featuring a strain gradient in the BHO layer, displays a significantly enhanced polarization of  $13.22 \mu\text{C cm}^{-2}$  at the same electric field - a 29-fold increase compared to the unstrained structure. The P-E loop of the strained system shows a deviation from ideal linear paraelectric behavior, characterized by an enclosed hysteresis area and relaxation behavior near the maximum applied field. Additional measurements conducted at

varying fields, frequencies, and temperatures (**Figure S5**) consistently confirm these trends. The STO/LBSO/BHO/LBSO device shows no signs of leakage up to an applied field of  $4.5 \text{ MV cm}^{-1}$  (**Figure S5 (a)**) and a frequency as low as 10 kHz (**Figure S5 (b)**). The STO/SRO/BHO/SRO device exhibits a significant noise, due to its low maximum polarization (**Figure S5 (d,e)**). In both cases, the measured polarization remains constant between temperatures of 450 K and 650 K (**Figure S5 (c,f)**).

This study demonstrates that engineering strain gradients in centrosymmetric, paraelectric BHO thin films can significantly enhance polarization responses through flexoelectric coupling. By comparing two capacitor structures - one with BHO coherently strained on LBSO electrodes and another with BHO fully relaxed on SRO electrodes - this work isolates the influence of strain gradients on the polar behavior of the material.

RSM and TEM analyses reveal that BHO grown on LBSO exhibits coherent epitaxial strain and a continuous strain gradient across its thickness. In contrast, BHO on SRO relaxes *via* misfit dislocations, resulting in a defect-rich interface. This structural difference correlates with the observed electrical properties: the strained BHO on LBSO shows a 29-fold increase in polarization and a fourfold enhancement in relative permittivity compared to the relaxed BHO on SRO. This is the first time such an increase in polar response is achieved in a centrosymmetric material by introducing a strain gradient. To date, prior studies have focused on the polar response in either ferroelectric materials or systems exhibiting strain-induced phase transitions.<sup>[17,20,21,34,35]</sup>

The observed increase in relative permittivity in the strained BHO/LBSO structure contrasts with some prior studies on ferroelectric materials, which report a reduction in dielectric response in the presence of strain gradients.<sup>[17]</sup> However, both interfacial strain and defect density can significantly

influence dielectric behavior. Interfacial defects are commonly associated with a suppression of permittivity due to scattering and disruption of lattice coherence, whereas coherent interfacial strain can enhance permittivity by altering the local polarizability and lattice dynamics.<sup>[36-41]</sup> Therefore, the enhanced polarizability observed here is likely the result of a complex interplay between the strain gradient, coherent interfacial strain, and the reduced defect density in the epitaxial BHO/LBSO system. Further experimental and theoretical work is necessary to decouple and quantitatively assess the individual contributions of these factors to the overall dielectric response.

The measured strain gradient of approximately  $10^6 \text{ m}^{-1}$  in the BHO/LBSO structure falls within the range known to produce significant flexoelectric polarization, as reported in previous studies on thin films.<sup>[1-3,17,20,21,42]</sup> However, the only centrosymmetric material studied is STO. Unlike STO, which can exhibit temperature and strain-dependent ferroelectric behavior, BHO remains paraelectric over a broad temperature range (50–800 K), in agreement with theoretical predictions.<sup>[24]</sup> The absence of any detectable phase transition in BHO throughout this range supports the conclusion that the observed polarization enhancement is attributable to strain gradient-induced flexoelectricity, not latent ferroelectricity or structural instabilities.<sup>[43-45]</sup> This is consistent with the understanding that flexoelectric effects can induce polarization in materials that are otherwise non-polar.<sup>[4,13-15]</sup>

## Conclusion

In summary, this work provides compelling evidence that strain gradient engineering via coherent epitaxial growth can effectively enhance the polar properties of centrosymmetric dielectrics through flexoelectric coupling. In this work, we have demonstrated the impact of strain gradient engineering on the polar properties of centrosymmetric, paraelectric BHO thin films by fabricating two capacitor structures *via* PLD: one incorporating a coherent BHO layer grown epitaxial on a LBSO bottom electrode (inducing a strain gradient), and another with a relaxed BHO layer grown on a mismatched SRO bottom electrode (without a significant strain gradient). RSM analysis confirms the presence of a substantial strain gradient ( $\sim 10^6 \text{ m}^{-1}$ ) in the BHO/LBSO heterostructure. Dielectric spectroscopy measurements revealed no phase transitions across a broad temperature range, confirming the intrinsic centrosymmetric and paraelectric nature of BHO. Remarkably, the strained BHO sample exhibited a 29-fold increase in polarization under an applied electric field of  $4 \text{ MV cm}^{-1}$ , alongside a significant enhancement in relative permittivity, compared to the relaxed counterpart. This provides the first direct experimental evidence of a strong correlation between an engineered strain gradient and enhanced polarization in a paraelectric perovskite oxide. Overall, this study establishes strain gradient engineering *via* coherent epitaxy as an efficient strategy for inducing and enhancing an electric polarization in non-polar materials through flexoelectric coupling. This approach offers a promising pathway for developing advanced dielectric materials and polar devices that do not rely on ferroic phase transitions.

## Experimental Section

### Pulsed Laser Deposition of the Thin Film Capacitor Structure

For each PLD process, a  $10 \times 10 \times 0.5$  mm<sup>2</sup> SrTiO<sub>3</sub> (100) substrate (Shinkosha) was used. The substrates were cleaned *via* sequential sonication: 10 min in acetone (Sigma-Aldrich), followed by 10 min in propan-2-ol (Sigma-Aldrich), and finally 30 min of chemical etching in a 1 M HCl solution in deionized water. After cleaning, the substrates were thermally annealed in a tube furnace (Heraeus AG) at 950 °C for 1 hour, with controlled heating and cooling rates of 6.2 °C min<sup>-1</sup> in an O<sub>2</sub> atmosphere. To ensure thermal contact during the PLD process, a 5 nm Ta adhesion layer followed by a 40 nm Pt layer were sputtered using a magnetron sputtering system (AJA).

Following annealing, the substrates were introduced into the PLD system (TSST) and heated at a rate of 10 °C min<sup>-1</sup> to the final deposition temperature. Thin films were fabricated using a pulsed KrF excimer laser (LPX305iCC, Lambda Physik) with a wavelength of 248 nm and a pulse length of 25 ns, ablating material from a disk-shaped target positioned 55 mm from the substrate with a spot size of 2.11 mm<sup>2</sup>. All targets were purchased from Ultimate Materials Technology Co., Ltd.

The LBSO bottom and top electrodes were deposited at 720 °C with a laser fluence of 1.50 J cm<sup>-2</sup>, an oxygen partial pressure of  $5 \times 10^{-2}$  mbar, a repetition rate of 2 Hz, and a total of 2000 pulses corresponding to a thickness of 40 nm. The SRO bottom and top electrodes were grown at 650 °C with an oxygen partial pressure of  $6 \times 10^{-2}$  mbar, a laser frequency of 1 Hz, a laser fluence of 2.00 J cm<sup>-2</sup> and 1800 pulses, corresponding to the same thickness as the LBSO. The BHO layer was deposited at 680 °C with a laser fluence of 1.75 J cm<sup>-2</sup>, an oxygen partial pressure of  $1 \times 10^{-2}$  mbar, a repetition rate of 5 Hz, and a total of 10,000 pulses, corresponding to a thickness of 100 nm. After deposition, the temperature was reduced at a rate of 10 °C min<sup>-1</sup> to room temperature while maintaining the oxygen partial pressure of the top electrode. Overall, two different capacitor systems were grown: STO/ LBSO/ BHO/ LBSO and STO/ SRO/ BHO/ SRO.

The growth was monitored *in situ* via a RHEED system (k-Space Associates, Inc.), operated at a emission current of 40 kV and an applied current of 1.5 A.

### Thin Film Morphology Characterization and Compositional Analysis

RSMs were performed using a Seifert 3003 PTS HRXRD equipped with a Cu K $\alpha$  radiation source ( $\lambda = 1.5406$  Å). The measurements were carried out using a line detector, which recorded intensity along  $2\theta$  with an angular resolution of 0.01°, and simultaneously employing an  $\omega$  step width of 0.01°. The exposure time for each step scan was set to 140 seconds to ensure sufficient signal-to-noise ratio. The sample alignment was performed with respect to the (-103) reflection of the STO substrate.

AFM measurements were performed using a NanoSurf FlexAFM operating in tapping mode equipped with NCLR-50 cantilevers (Nano World). Images were acquired at a resolution of  $512 \times 512$  pixels with a line scan time of 4 seconds.

TEM investigations were performed on a probe-corrected JEOL JEM ARM-200F (NeoARM), operated at 200keV and equipped with a cold-field emission gun and two energy dispersive X-

ray spectroscopy detectors by JEOL. The TEM lamella was prepared by focused Ga-ion beam (Ga-FIB; Zeiss NVision40). First, a protection layer was grown by e-beam assisted deposition (C-deposition followed by Pt-deposition), which was finally covered by a thick carbon layer grown by Ga-ion assisted deposition. The lamella was then prepared using a beam of 80 pA at 30 keV for final polishing. Both TEM specimen preparation and investigations were performed by the EMF team at PSI.

The film composition was analyzed by RBS using a 2 MeV He<sup>+</sup> ion beam at the Laboratory of Ion Beam Physics, ETH Zurich. The acquired spectra were evaluated using SIMNRA 7 simulations.

### **Electrode Fabrication and Patterning**

The top electrode geometry was defined using a photolithographic process with a positive photoresist (S1813 G2, Kayaku Advanced Materials). The photoresist was spin-coated onto the sample at 3000 rpm for 60 seconds, followed by a soft bake at 137°C for 60 seconds to enhance adhesion and uniformity. A direct-write lithography system was used to define circular electrode patterns with a diameter of 75 μm, 50 μm and 25 μm, by selectively leaving these areas unexposed to UV radiation. The exposed photoresist regions were subsequently dissolved using a developer solution (AZ 726 MIF, Merck), leaving only the masked electrode areas protected.

After development, ion-beam etching (IBE) was used to remove the uncovered top layer material, defining the electrode structures, using either one of the following methods. Ar-ion beam etching was performed on patterned samples either with an Electrostatic Quadrupole Secondary Ion Mass Spectrometer (SIMS) (EQS-MS, Hiden Analytical Ltd.) or an Ionfab system (Oxford Instruments). In the former instrument, the sample was etched using a focused Ar<sup>+</sup> beam of ~100 μm diameter with an ion energy of 2.5 kV (-107 nA ion beam current) within an area of 2000×2000 μm<sup>2</sup>. The selected spatial resolution was 400×400 pixels to keep a balance between etching speed and depth resolution. In order to distinguish the interface between LBSO and BHO, La<sup>+</sup>, Ba<sup>+</sup> and Hf<sup>+</sup> were measured by the mass spectrometer during the etching process. An electron flood source (FS40, PREVAC) was used for charge compensation during the etching process. In the latter instrument, an 8 sccm Ar gas flow and an Ar<sup>+</sup> beam voltage of 250 V were used, corresponding to a beam current of 30 mA. During etching, the sample was rotated at 20 rpm and tilted at a 15° angle relative to the incident ion beam. The sample was etched for 10 min, corresponding to an etching depth of 40 nm (the thickness of the top electrode layer). The remaining photoresist was then removed using acetone. For the bottom contact, Ag paste (Sigma-Aldrich) was applied to ensure a reliable electrical connection.

### **Dielectric Function and Polarization-Electric Field Hysteresis Measurements**

The dielectric and P-E hysteresis measurements were performed using a cryogenic probe station (Advanced Research Systems) to ensure temperature stability and minimize external influences. The dielectric constant was measured using a Precision LCR Meter (E4980A, Keysight). A small AC voltage of 60 mV (corresponding to a field of 60 kV/cm) was applied to the sample, and measurements were conducted over a frequency range from  $2 \times 10^2$  Hz to  $2 \times 10^6$  Hz. The data acquisition was performed at 200 logarithmically spaced frequency points, with each point

representing the average of five consecutive measurements to improve accuracy. For P-E hysteresis measurements, a Radiant Precision Multiferroic materials analyzer was used. The hysteresis loops were recorded with a measurement speed of 1 ms and a preset delay of 1000 ms to ensure charge stabilization. A total of 2000 measurement points were taken for each loop to accurately capture the polarization response.

### **Acknowledgements**

The authors wish to acknowledge funding from the Swiss National Science Foundation (SNSF) as part of an Ambizione fellowship (216196) and the project funding scheme (204103). We acknowledge the usage of the instrumentation provided by the Electron Microscopy Facility at PSI and we thank the EMF team for their help and support. JAB acknowledges funding from the European Union's Horizon 2020 research and innovation programme under the Marie Skłodowska-Curie grant agreement No 884104 (PSI-FELLOW-III-3i). We thank the staff of the Laboratory for Nano and Quantum Technologies (LNQ) at PSI for cleanroom support.

### **Conflict of Interest**

The authors declare no conflict of interest.

## References

- [1] P. Zubko, G. Catalan, A. K. Tagantsev, *Annual Reviews of Materials Research* 2013, **43**, 387–421.
- [2] D. Lee, B. C. Jeon, A. Yoon, Y. Jae Shin, M. H. Lee, T. K. Song, S. D. Bu, M. Kim, J. Chung, J. Yoon, T. W. Noh, *Adv. Mater.* 2014, **26**, 5005–5011.
- [3] Z. Wang, C. Li, Z. Zhang, Y. Hu, W. Huang, S. Ke, R. Zheng, F. Li, L. Shu, *Scripta Mater.* 2022, **210**, 114427.
- [4] N. A. Pertsev, A. K. Tagantsev, N. Setter, *Phys. Rev. B* 2000, **65**, 219901.
- [5] Q. Deng, S. Lv, Z. Li, K. Tan, X. Liang, S. Shen, *J. Appl. Phys.* 2020, **128**, 080902.
- [6] Z. Wang, C. Li, H. Xie, Z. Zhang, W. Huang, S. Ke, L. Shu, *Phys. Rev. Appl.* 2022, **18**, 064017.
- [7] D. Rasic and J. Narayan, *Crystal Growth IntechOpen*, **2019**.
- [8] N. A. Shepelin, Z. P. Tehrani, N. Ohannessian, C. W. Schneider, D. Pergolesi, T. Lippert, *Chem. Soc. Rev.* 2023, **52**, 2294.
- [9] Y. Sun, J. Yang, S. Li, D. Wang, *Chem. Commun.* 2021, **57**, 8402–8420.
- [10] J. Narayan and S. Sharan, *Mater. Sci. Eng. B* 1991, **10**, 261–267.
- [11] X. Ren, K. Otsuka, *Phys. Rev. Lett.* 2000, **85**, 5.
- [12] V. S. Mashkevich, K. B. Tolpygo, *Sov. Phys. JETP* 1957, **4**, 435–439.
- [13] S. M. Kogan, *Sov. Phys. Solid State* 1964, **5**, 2069–2070.
- [14] A. K. Tagantsev, *Sov. Phys. JETP* 1985, **61**, 1246–1254.
- [15] A. K. Tagantsev, *Phys. Rev. B* 1986, **34**, 5883–5889.
- [16] P. Zubko, G. Catalan, A. Buckley, P. R. L. Welche, J. F. Scott, *Phys. Rev. Lett.* 2007, **99**, 167601.
- [17] G. Catalan, B. Noheda, J. McAneney, L. J. Sinnamon, J. M. Gregg, *Phys. Rev. B* 2005, **72**, 020102.
- [18] M. A. Peña, J. L. G. Fierro, *Chem. Rev.* 2001, **101**, 1981–2017.
- [19] L. W. Martin, Y.-H. Chu, R. Ramesh, *Mater. Sci. Eng. R* 2010, **68**, 89–133.
- [20] D. Lee, A. Yoon, S. Y. Jang, J.-G. Yoon, J.-S. Chung, M. Kim, J. F. Scott, T. W. Noh, *Phys. Rev. Focus* 2011, **28**, 5.
- [21] D. Lee, S. M. Yang, J.-G. Yoon, T. W. Noh, *Nano Lett.* 2012, **12**, 6436–6440.
- [22] H. Zhao, A. Chang, Y. Wang, *Physica B Condensed Matter* 2009, **16**, 2192–2196.
- [23] C. Gattinoni, N. A. Spaldin, *Physical Review Research* 2022 **4**, L032020
- [24] Y. M. Kim et al., *APL Mater.* 2017, **5**, 016104.
- [25] C.-H. Ma, Y.-K. Liao, Y. Zheng, S. Zhuang, S.-C. Lu, P.-W. Shao, J.-W. Chen, Y.-H. Lai, P. Yu, J.-M. Hu, R. Huang, Y.-H. Chu, *ACS Appl. Mater. Interfaces* 2022, **14**, 22278–22286.
- [26] H. F. Poulsen, P. K. Cook, H. Leemreize, A. F. Pedersen, C. Yildirim, M. Kutsal, A. C. Jakobsen, J. X. Trujillo, J. Ormstrup, C. Detlefs, *J. Appl. Cryst.* 2018, **51**, 1428-1436
- [27] W.-X Ni, K Lyutovich, J Alami, C Tengstedt, M Bauer, E Kasper, *J. Cryst. Growth* 2001, **227-228**, 756-760

- [28]M. Labardi, M. Lucchesi, D. Prevosto, S. Capaccioli, *Appl. Phys. Lett.* 2016, **108**, 182906.
- [29]M. David, Y. Feldman, P. B. Ishai, *Non-Destructive Material Characterization Methods* Elsevier, **2024**.
- [30]R. J. D. Tilley, *Nature* 1977, **269**, 229–231.
- [31]T. R. Taylor, P. J. Hansen, N. Pervez, B. Acikel, R. A. York, J. S. Speck, *J. Appl. Phys.* 2003, **94**, 3390–3396.
- [32]A. Tkach, P. M. Vilarinho, A. M. R. Senos, A. L. Kholkin, *J. Eur. Ceram. Soc.* 2005, **25**, 2769–2772.
- [33]C. Lee et al., *Appl. Phys. Lett.* 2013, **102**, 082905.
- [34]P. Yudin, J. Duchon, O. Pacherova, M. Klementova, T. Kocourek, A. Dejneka, and M. Tyunina. *Phys. Rev. Research* 2021, **3**, 033213.
- [35]S. Li, Y. Wang, M. Yang, S. Xu, M. Liu, Q. Li, J. Miao, E.-J. Guo, K. Jin, L. Gu, Q. Zhang, J. Deng, X. Chen, X. Xing. *Chem. Mater.* 2023, **35**, 2967–2974.
- [36]C. L. Canedy, Hao Li, S. P. Alpay, L. Salamanca-Riba, A. L. Roytburd, R. Ramesh. *Appl. Phys. Lett.* 2000, **77**, 1695–1697
- [37]M.-W. Chu, I. Szafraniak, R. Scholz, C. Harnagea, D. Hesse, M. Alexe, U. Gösele. *Nature Materials* 2004, **3**, 87–90
- [38]L. Ryen, X. Wang, P. Petrov, E. Carlsson, U. Helmersson, E. Olsson. *J. Appl. Phys.* 1999, **85**, 3976–3983
- [39]I. Vrejoiu, J. D. Pedarnig, D. Bäuerle, M. Dinescu. *Appl. Phys. Lett.* 2003, **83**, 2130–2132
- [40]S. Hyun, K. Char. *Appl. Phys. Lett.* 2001, **79**, 254–256
- [41]K. V. L. V. Narayanachari, H. Chandrasekarm, A. Banerjee; K. B. R. Varma, R. Ranjan, N. Bhat, S. Raghavan. *J. Appl. Phys.* 2016, **119**, 014106
- [42]S. Cai, Y. Lun, D. Ji, P. Lv, L. Han, et al. *Nature communications* 2022 **13**, 5116
- [43]M. I. Khan, T. C. Upadhyay, *Multifunctional Ferroelectric Materials* Springer, 2021.
- [44]G. G. Guzmán-Verri, P. B. Littlewood, C. M. Varma, *Phys. Rev. B* 2013, **88**, 134106.
- [45]W. F. Brown Jr., *Dielectrics* Springer, **1956**.

# Supporting Information

## Flexoelectric Polarization Enhancement in Paraelectric BaHfO<sub>3</sub> via Strain Gradient Engineering

*Timo Piecuch<sup>1,2</sup>, Jeffrey A. Brock<sup>1,3</sup>, Xiaochun Huang<sup>1,2</sup>, Arnold M. Müller<sup>4</sup>, Christof Vockenhuber<sup>4</sup>, Christof W. Schneider<sup>1</sup>, Thomas Lippert<sup>1,2</sup>, Nick A. Shepelin<sup>1\*</sup>*

<sup>1</sup>Center for Neutron and Muon Sciences, Paul Scherrer Institute, 5232 Villigen PSI, Switzerland

<sup>2</sup>Laboratory of Inorganic Chemistry, Department of Chemistry and Applied Biosciences, ETH Zürich, 8093 Zurich, Switzerland

<sup>3</sup>Laboratory for Mesoscopic Systems, Department of Materials, ETH Zürich, 8093 Zurich, Switzerland

<sup>4</sup>Laboratory of Ion Beam Physics, ETH Zürich, 8093, Zürich, Switzerland

## S1: Growth Quality

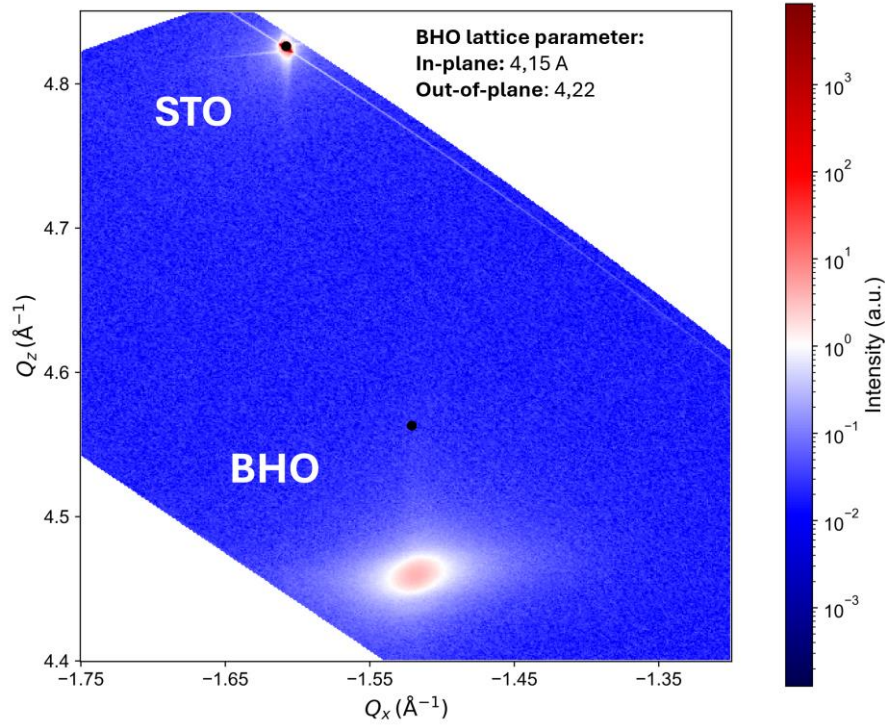


**Figure S1.** RSM of the asymmetrical (-103) signal of BHO directly grown on the STO substrate. The black dots indicate the literature positions of STO and BHO bulk materials. BHO is fully relaxed in-plane, due to a lattice mismatch of 6.8 % between substrate and film and the lack of overlap between the two peaks in  $Q_x$ . The in-plane and out-of-plane lattice parameters of BHO are indicated.

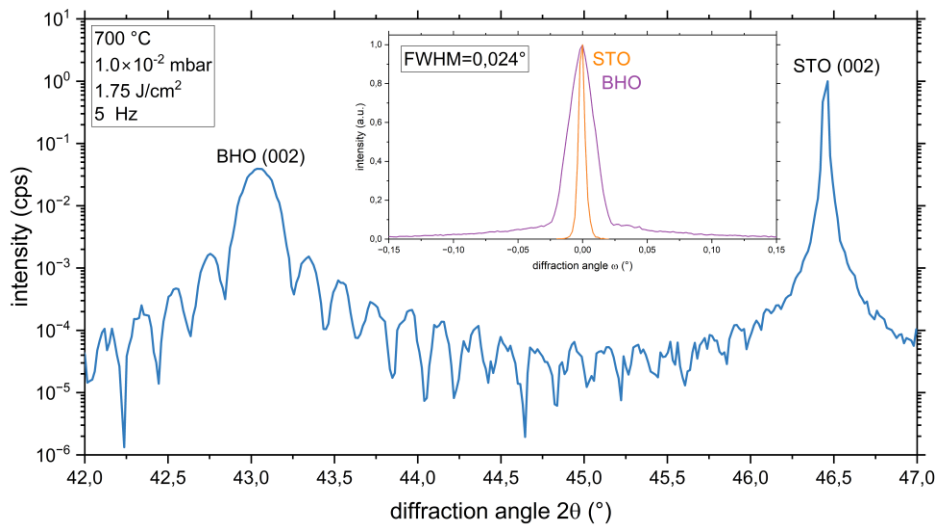
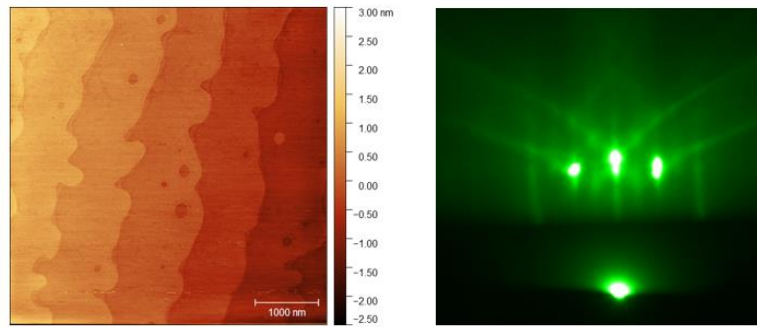


**Figure S2.** XRD  $2\theta$  line-scan of the 50 nm thick BHO grown on STO. The inset shows the rocking curve for the film and the substrate. Film full width at half maximum (FWHM) and growth parameters are indicated.

Substrate:  
SrTiO<sub>3</sub> (STO)



Film (50nm):  
BaHfO<sub>3</sub> (BHO)

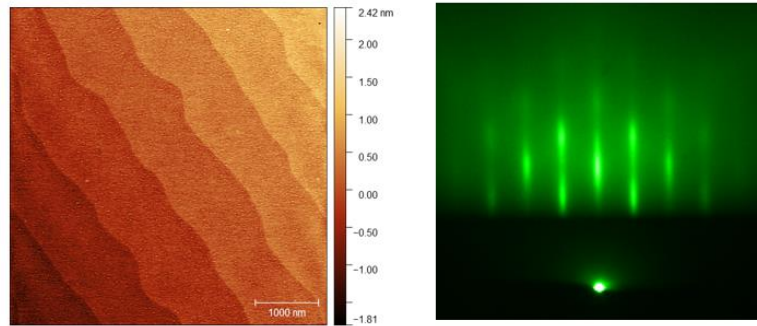


**Figure S3.** (left) AFM topography ( $5 \times 5 \mu\text{m}$ ) and (right) RHEED pattern before (top) and after (bottom) deposition of the 50 nm BHO film on the STO substrate employing the best growth conditions. The AFM data displays evenly spaced terrace steps, and the RHEED pattern shows streaks,

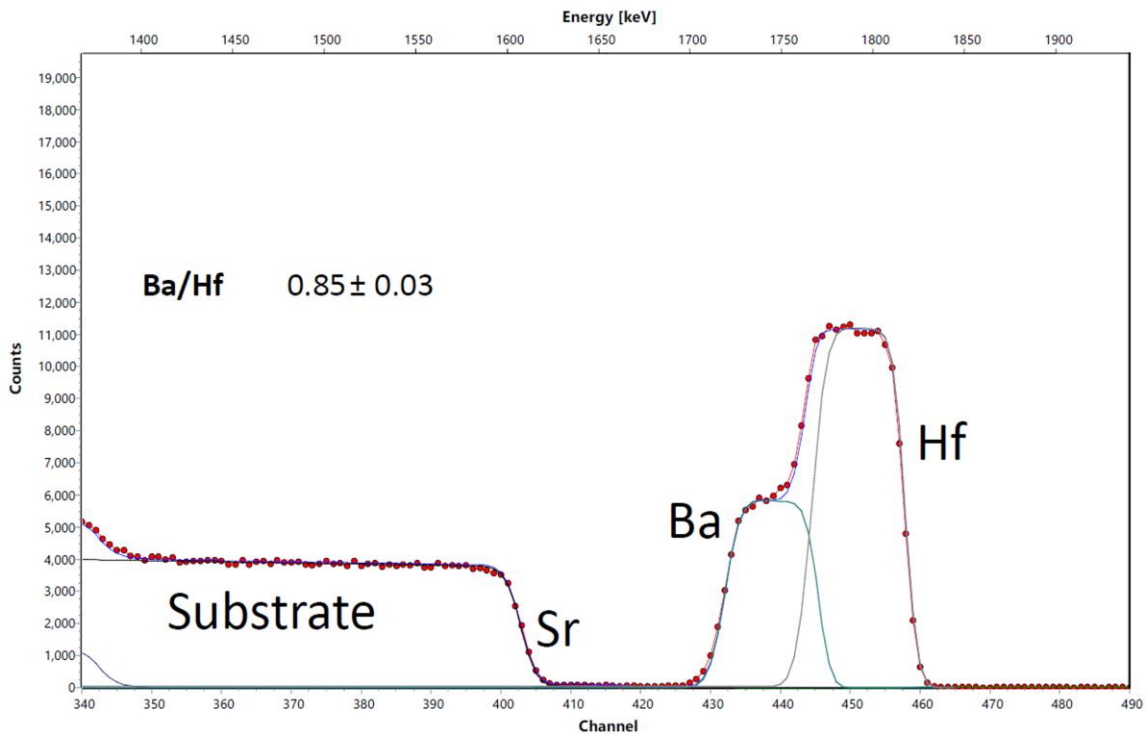


**Figure S4.** RBS spectra of the 50 nm BHO film grown on the STO substrate. Elemental cation ratio is indicated, exposing a Ba deficiency.

## S2: Electrical Properties

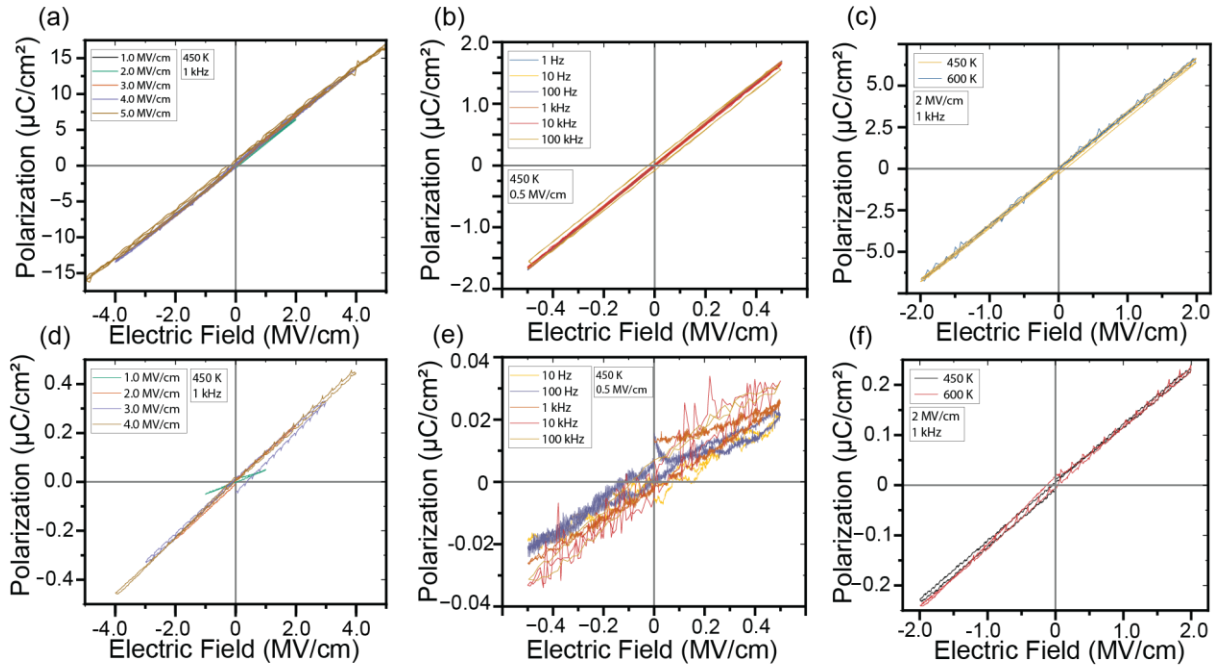


**Figure S5.** P-E hysteresis for the STO – SRO – BHO – SRO structure (a-c) and the STO – LBSO – BHO – LBSO structure (d-f). The measurements have been performed for different fields (a,d), different frequencies (b,e) and different temperatures (c,f).